Journal of Tissue Engineering
Volume 13: 1–11

DOI: 10.1177/20417314221108791
journals.sagepub.com/home/tej
SAGE

Tissue-engineered composite tracheal grafts create mechanically stable and biocompatible airway replacements

Lumei Liu[1], Sayali Dharmadhikari[1,2], Barak M Spector[3], Zheng Hong Tan[4], Catherine E Van Curen[3], Riddhima Agarwal[4], Sarah Nyirjesy[3,4], Kimberly Shontz[1], Sarah A Sperber[1], Christopher K Breuer[1,5], Kai Zhao[3], Susan D Reynolds[6], Amy Manning[2,3,4], Kyle K VanKoevering[3,4] and Tendy Chiang[1,2,3,4]

Abstract

We tested composite tracheal grafts (CTG) composed of a partially decellularized tracheal graft (PDTG) combined with a 3-dimensional (3D)-printed airway splint for use in long-segment airway reconstruction. CTG is designed to recapitulate the 3D extracellular matrix of the trachea with stable mechanical properties imparted from the extraluminal airway splint. We performed segmental orthotopic tracheal replacement in a mouse microsurgical model. MicroCT was used to measure graft patency. Tracheal neotissue formation was quantified histologically. Airflow dynamic properties were analyzed using computational fluid dynamics. We found that CTG are easily implanted and did not result in vascular erosion, tracheal injury, or inflammation. Graft epithelialization and endothelialization were comparable with CTG to control. Tracheal collapse was absent with CTG. Composite tracheal scaffolds combine biocompatible synthetic support with PDTG, supporting the regeneration of host epithelium while maintaining graft structure.

Keywords

Composite tracheal graft, partially decellularized tracheal scaffold, 3D-printed splint, tracheal collapse, tissue regeneration

Date received: 2 March 2022; accepted: 7 June 2022

Introduction

Despite advances in airway surgery, the optimal management of long-segment tracheal defects remains undiscovered.[1–3] The lack of cure stems from the need for replacement tissue but no suitable autologous, biologic, or synthetic source for the trachea has been identified.[4] Regenerative medicine and tissue engineering have the potential to create biocompatible grafts for tracheal reconstruction by creating organ replacements that are identical to native tissue. Within regenerative medicine, decellularization represents the first successful clinical translation within the field. Decellularized allografts can provide native biophysical and biochemical cues that promote regeneration and are non-immunogenic.[5,6] Unfortunately, when applied to

[1]Center of Regenerative Medicine, Abigail Wexner Research Institute, Nationwide Children's Hospital, Columbus, OH, USA
[2]Department of Pediatric Otolaryngology, Nationwide Children's Hospital, Columbus, OH, USA
[3]Department of Otolaryngology-Head & Neck Surgery, The Ohio State University Medical Center, Columbus, OH, USA
[4]College of Medicine, The Ohio State University, Columbus, OH, USA
[5]Department of Pediatric Surgery, Nationwide Children's Hospital, Columbus, OH, USA
[6]Center for Perinatal Research, Abigail Wexner Research Institute, Nationwide Children's Hospital, Columbus, OH, USA

Corresponding author:
Tendy Chiang, Center of Regenerative Medicine, Abigail Wexner Research Institute, Nationwide Children's Hospital, 555 S. 18th Street, Suite 2A, Columbus, OH 43205-2664, USA.
Email: Tendy.Chiang@nationwidechildrens.org

tracheal grafts, conventional decellularization can result in significant collapse due to loss of mechanical properties, extracellular matrix, and glycosaminoglycans.[7–11] In recent years, the concept of *partial* decellularization has been adopted for the trachea, leveraging the morphologically distinct regions of immunogenicity of the trachea. Partial decellularization removes the highly immunogenic epithelium and lamina propria while preserving immune-privileged cartilage.[12,13] Consequently, a partially decellularized tracheal allograft permits transplantation in the absence of immunosuppression while providing a scaffold capable of rapid host-derived regeneration.

We demonstrated that partially decellularized tracheal grafts (PDTG) can sustain host-derived epithelialization and endothelialization while supporting graft chondrocyte viability.[7,12,14–16] Despite rapid neotissue formation, one of the predominant complications of any airway reconstruction surgery is stenosis or collapse of the surgically corrected airway.[8,11,17,18] We assessed the performance of composite tracheal grafting, creating a hybrid graft composed of PDTG combined with external splinting. We assess the performance of Composite Tracheal Grafts (CTG) in a mouse model of orthotopic tracheal replacement.

Materials and methods

Animal care and ethics statement

The Institutional Animal Care and Use Committee of the Abigail Wexner Research Institute at Nationwide Children's Hospital (Columbus, OH) reviewed and approved the protocol (AR15-00090). All animals received humane care according to the standards published by the Public Health Service, National Institutes of Health (Bethesda, MD) in the Care and Use of Laboratory Animals (2011), and US Department of Agriculture (USDA) regulations outlined in the Animal Welfare Act.

Fabrication of syngeneic, partially decellularized and conventionally decellularized tracheal grafts (STG, PDTG, and CDTG)

Tracheal grafts were harvested from 6 to 8-week-old C57BL/6J female mice as previously described.[19,20] Proximal tracheas were dissected, and a 5 mm tracheal segment was harvested and immersed in phosphate-buffered saline (PBS, Gibco, Thermo Fisher Scientific, Waltham, WA) before implantation. STG were implanted following harvest without additional processing.

PDTG were prepared as previously published.[7] Briefly, harvested tracheas were rinsed with 1X PBS with 1% penicillin/streptomycin (P/S, Gibco, Thermo Fisher Scientific, Waltham, MA), then treated with 0.01% (w/v) sodium dodecyl sulfate solution (SDS, Sigma-Aldrich, MO) for 5 min. Tracheas were washed with 0.9% sodium chloride (NaCl, Fisher Scientific, Fair Lawn, NJ) solution three times for progressive 10-, 15-, and 20-min sessions. Then, the tracheal segments were treated with 0.01% (w/v) and 0.1% (w/v) SDS solutions for 24 h each, 0.2% and 0.1% SDS was used for 3 h of treatment each. Nucleic acid content was removed using 1% Triton X-100 solution for 30 min. Grafts were immersed in 0.9% NaCl solution overnight at 4°C. All steps were performed on a shaking platform set to 48 rounds/min.

As a control, conventionally decellularized tracheal grafts (CDTG) were created following published decellularization protocols.[21] Harvested tracheas were immersed in an incubation solution containing 10 mM Tris buffer (pH 8.0), 0.1% ethylenediaminetetraacetic acid (EDTA; Calbiochem®, Sigma-Aldrich, St. Louis, MO) and 10 kIU/mL aprotinin (Sigma-Aldrich) for 1 h. Tracheas were then decellularized with 0.1% SDS in hypotonic 10 mM Tris buffer with 0.1% Ethylenediaminetetraacetic acid (EDTA) and 10 kIU aprotinin at room temperature on a shaking platform (150 rounds/min). Solutions were replenished every 12 h for 2 days. After decellularization, tracheas were washed six times in PBS for 10 min each time, then transferred into a solution of 20 mg/mL RNase A (Sigma-Aldrich) and 0.2 mg/mL DNase (Sigma-Aldrich) in 4.2 mM magnesium sulfate (Sigma-Aldrich), 5 mM Ca^{2+} (Sigma-Aldrich), and Tris-HCl buffer (pH 7.2). Agitation continued for an additional 2 days with the solution changed every 12 h. Finally, decellularized tracheas were washed with six 10-min rinses of PBS. Grafts were stored in PBS at −20°C.

DNA quantification

Up to four grafts from each method were processed for DNA quantification (DNeasy Blood & Tissue Kit, QIAGEN, MI) to evaluate decellularization efficiency. Native tracheal grafts and PDTG were weighed prior to assay. The DNA extraction process followed the manufacturer's specifications.[22] DNA concentration was measured using the Nanodrop™ 2000c spectrophotometer (Thermo Fisher Scientific, Waltham, MA).

Mechanical testing of mouse tracheal grafts

There is no commercially available material testing system that can measure the compressive force of mouse trachea. We created a method of quantifying the stiffness of mouse trachea with the use of static compression in conjunction with image processing. Tracheal grafts were placed on glass slides with the trachealis muscle oriented on the slide. The lumen was visualized to permit visualization of uniaxial compression with a high-definition camera while passive weights were placed on the anterior trachea. Images of the tracheal lumen were captured after application of the weights, and the resultant displacement was quantified using ImageJ software (ImageJ, NIH, Bethesda,

Maryland). Stiffness was calculated by dividing displacement by the weight of compression. Four replicates of native and PDTG groups were tested.

Splint fabrication

MicroCT images of a dissected mouse trachea were utilized to create a 3D model of the tracheal anatomy. Based on this 3D model, external airway splints were designed in Solidworks (Solidworks 2021, Dassault Systems, France) to encircle 270° around the trachea, sparing the posterior wall.[23] The length of the splint was designed to span a 3 mm defect, with additional length to overlap the native trachea at each end. A 3 × 3 scaffold design was incorporated to allow the external splint to be secured with sutures to both the graft and native trachea, providing radial traction to maintain graft patency. Wall thickness of the external splint was set to 250 μm.

Splints were then manufactured via stereolithography (SLA) 3D Printing (Form3B, FormLabs, Somerville, MA) in a biocompatible resin polymer (BioMed Amber). Splints were post-processed in standard fashion, and autoclave sterilized for implantation according to the protocol set forth for the material used. Mechanical properties of the splint could not be quantified with our methods (Section 2.4) given that the stiffness of the splint exceeded the passive compressive force of the system.

Implantation of 3D printed tracheal splints

STG were implanted into C57BL/6J mice as previously described.[20] Briefly, the airway was dissected free from adjacent structures. A 3–4 mm segment was resected and orthotopically implanted. The 3D-printed splints (Section 2.5) were implanted on the intact trachea and STG. Briefly, 9–0 sterile nylon sutures were first passed around the rings of the implanted graft, securing the splint to the midpoint of the graft. The ends of the splint were then secured to the proximal and distal native airway. Grafts were explanted at 3 months to evaluate for local tissue response as well as chronic inflammation (N = 5/group).

Implantation of PDTG and CTG

PDTG were implanted following previously published methods.[20,24] A 3D-printed tracheal splint was then implanted on PDTG, creating a composite tracheal graft (CTG) as described in Section 2.6. Radiopaque markers were secured at the distal and proximal anastomoses to identify the boundaries of the graft during micro-computed tomography (microCT). Mice were randomly assigned to experimental groups (N = 8 for STG, N = 28 for PDTG, N = 16 for CTG). Animals were closely monitored for early (humane) euthanasia criteria including respiratory distress (labored breathing, stridor) and/or more than 20% weight loss compared to weight before surgery. At planned (d28 post-op) or humane endpoint, animals were euthanized with a ketamine/xylazine cocktail overdose. Once euthanasia was confirmed, the graft and flanking host tissue was recovered and fixed in 10% neutral-buffered formalin (NBF).

Histology

PDTG, CDTG, and CTG were fixed in 10% NBF at room temperature for 24–48 h. Paraffin-embedded samples were sectioned into 4 μm thickness both axially and longitudinally. De-paraffinized and rehydrated sections were stained with hematoxylin (Sigma-Aldrich, MO) and counterstained with eosin to visualize decellularization. Pre-implant tracheal grafts were evaluated for glycosaminoglycan content (GAG) using Alcian blue staining and total collagen using Masson's Trichrome staining (Sigma-Aldrich). Epithelialization was assessed with hematoxylin and eosin (H&E) stain of post-implantation tracheal sections. Images of stained sections were captured using bright field microscopy (Zeiss, Oberkochen, Germany). Submucosal thickness was quantified using ImageJ software and calculated by averaging 5 measurements on each graft cartilage ring. Previous work has demonstrated host-derived myeloid cells as the major population infiltrating the lamina propria and mediating the chronic inflammatory response in tracheal grafts resulting in stenosis.[19,20,25–30] Immunohistochemistry (IHC) was performed to examine macrophage (pan, M1, and M2) distribution (CD68, CD206, iNOS respectively) using methods described previously as this is one of the most prevalent myeloid cell type seen in implanted tracheal grafts.[31,32] Immunofluorescent (IF) staining for epithelial (ACT, CCSP, K5/K14) and endothelial (CD31) biomarkers was completed using previously described methods.[7,19]

Micro-computed tomography (microCT)

MicroCT was performed on postoperative days 0, 3, and 7 as previously described (N = 4 for STG, N = 14 for PDTG, N = 8 for CTG).[33] In vivo imaging was performed with the Trifoil eXplore Locus RS 80: animals were positioned prone in the microCT chamber under inhalational anesthesia (1%–3% isoflurane in room air at 1–3 L/min). For terminal scans at planned end time point (28 days) and early humane euthanasia (EE) time points, mice were euthanized before imaging. All scans had full resolution reconstruction, producing 45 μm sections for living animal scan and 20 μm sections following euthanasia. The host and graft airway were evaluated in the sagittal plane. The minimal luminal diameter of the graft and native airway was obtained using image processing software. MicroCT scans were then reconstructed and segmented to assess with computational fluid dynamics (CFD) using Amira software (Thermo Fisher Scientific). A commercial grid generator

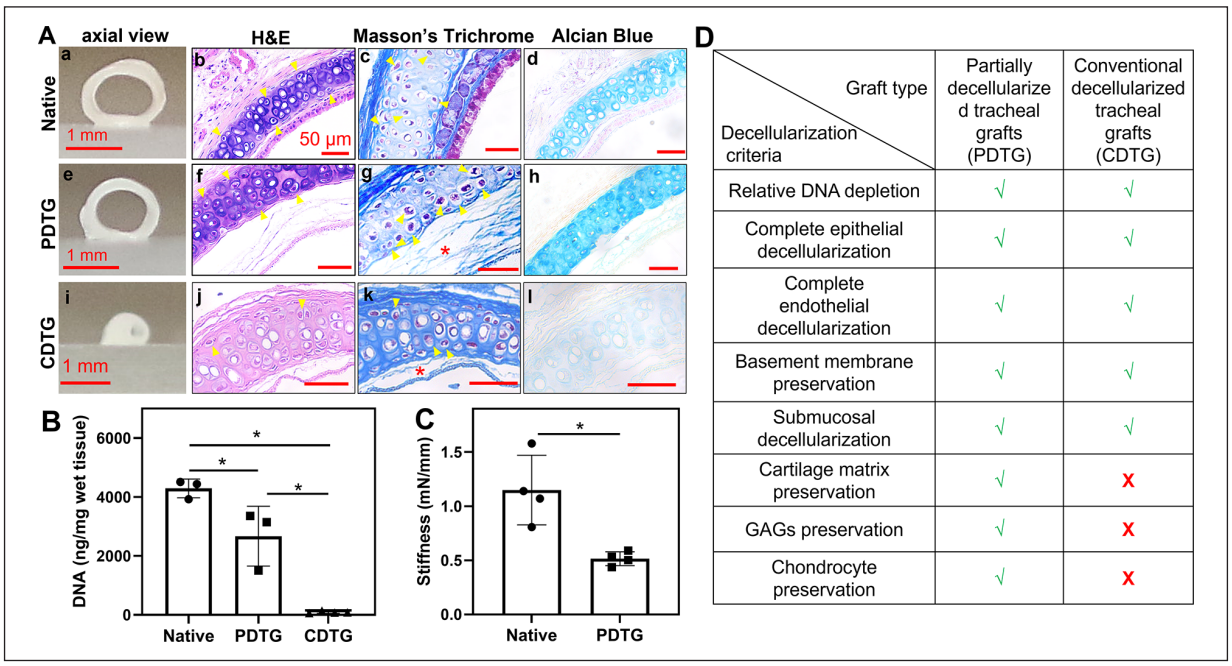

Figure 1. The impact of decellularization on graft composition, histology, and biomechanics. (A) Gross axial images of grafts (a, e, and i), H&E (b, f, and j), Masson's Trichrome (collagen), and Alcian blue (GAG) of native trachea (control) (a–d), PDTG (e–h), and CDTG (i–l). (B) DNA amount (ng/mg) in native trachea, PDTG, and CDTG; * represent significant decrease of DNA amount ($p = 0.0296$ for native vs PDTG, $p < 0.0001$ for native vs CDTG, $p = 0.0202$ for PDTG vs CDTG). (C) tracheal stiffness (mN/mm) of native trachea and PDTG. * denote lower stiffness of PDTG than native trachea ($p = 0.0266$, testing was not feasible for the CDTG group due to complete collapse). (D) Metrics assessed in PDTG and CDTG.

ICEM CFD was applied to generate a computational mesh, separating the inlet and outlet of the 3D trachea. Inspiratory turbulent airflow was stimulated by applying a target flow rate based on mouse weight and tidal volume. Normalized average velocity, peak wall shear stress (WSS), and resistance were recorded for selected subjects ($N = 3$/group) at critical time points.

Statistical analysis

Normally distributed data were compared using Welch's *t*-test for data with non-equal variances and unpaired *t*-test for data with equal variances. Non-parametric tests (Mann-Whitney) were used for data that were not distributed normally. Statistical tests were performed using the GraphPad Prism 8 software (GraphPad Software Inc., CA). Statistical difference was defined as $p < 0.05$. Experimental data were expressed as mean ± standard deviation (SD). CFD quantification was expressed as mean ± standard error of the mean (SEM).

Results

Partial decellularization removes epithelial cells while preserving graft cartilage and patency

PDTG retained gross graft patency when compared to CDTG, which demonstrated a complete loss of native tracheal structure and shape (Figures 1(a), (e), and (i)). There was a depletion of epithelial and submucosal cells in both PDTG and CDTG on H&E with a reduction of hematoxylin staining in the cartilage extracellular matrix (ECM) of CDTG indicating a loss of the territorial matrix (Figures 1(a), (f), and (j)). Collagen (Masson's Trichrome) was preserved in PDTG compared to disruptions seen in the lamina propria of CDTG (red *, Figures 1(a), (g), and (k)). Glycosaminoglycans (Alcian Blue) were dramatically depleted in CDTG compared to their relative preservation in PDTG (Figures 1(a), (h), and (l)). PDTG and CDTG resulted in DNA depletion and CDTG showed a greater degree of decellularization than PDTG (Figure 1(b)). PDTG was less stiff than native trachea (*, Figure 1(c)). CDTG stiffness was not able to be measured due to complete collapse before compression. The metrics assessed in PDTG and CDTG are summarized in Figure 1(d).

A 3D-printed tracheal splint can be implanted with segmental tracheal replacement and does not cause airway erosion or chronic inflammation

3D-printed tracheal splints were designed to match the dimensions of the mouse trachea. Splints were printed with surgical guide resin, a non-resorbable, inert

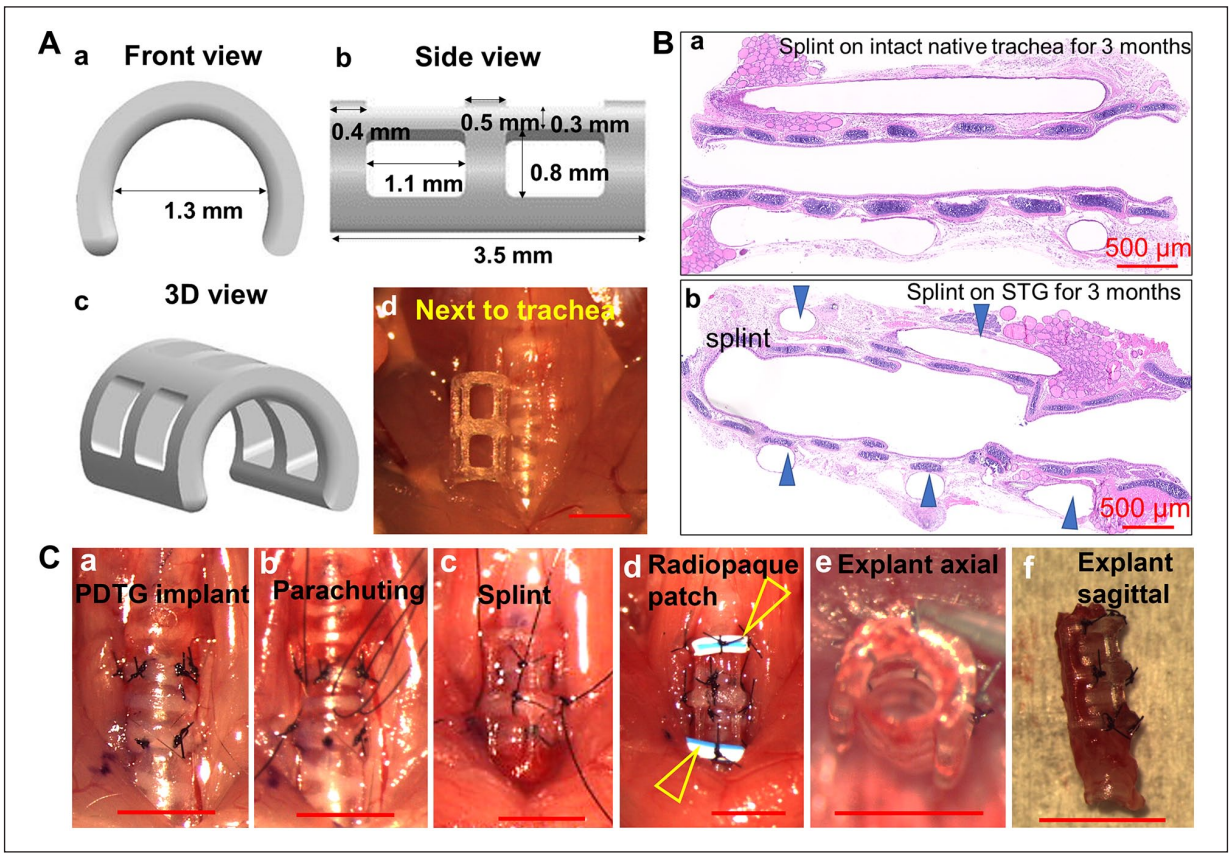

Figure 2. Splint, PDTG, and CTG implantation. (A) Rendering of splint design in front (a) and side view (b), 3D view (c), and approximation of mouse trachea (d). (B) Representative H&E images of splint implantation for 3 months to demonstrate a lack of chronic inflammation on the native trachea (a) and STG (b). Arrowheads denote the splint. (C) PDTG and CTG implantation procedure (a–d), and the axial (e) and sagittal (f) view of CTG following explanation at day 0.

polymer to deliver consistent mechanical support throughout the duration of the experimental period (3 months). Twelve prototypes were examined for implant potential. Prototype design included variations in diameter (1.3, 1.5, 1.7 mm), length (2, 4 mm), and suture site placement (gross images, Supplemental Figure S1). Different prototypes were placed onto the mouse trachea in vivo and evaluated for fit over both the native trachea and tracheal grafts. The ideal dimensions for the mouse model were identified as a splint with a 1.3 mm inner diameter and 3.5 mm length, and with square suture placement sites that could externally span tracheal grafts (Figure 2(a)).

The long-term effects of the splint were assessed in vivo. Splints were implanted on native trachea and in conjunction with orthotopic tracheal replacement with syngeneic tracheal grafts. No early mortality was observed, and grafts were explanted at 3 months. There was no evidence of vascular erosion, airway injury, or anastomotic disruption. In addition, there were no signs of encapsulation and eosinophilic infiltration indicative of chronic inflammation (Figure 2(b)). CTG were then implanted to access in vivo performance for 1 month (Figure 2(a)–(d)) and were found to retain native tracheal dimensions (Figures 2(c) and (f)).

Implantation and survival

Of the four CDTG grafts, none were viable for implantation due to loss of native tracheal structure and shape, therefore they were excluded from in vivo analysis. Eight mice were included in the STG group, with one requiring early euthanasia. Of the 28 mice in the PDTG group, 17 required EE, and 11 survived to the 28-day endpoint. Finally, 16 mice were included in the CTG group with 8 requiring EE and 8 surviving to the 28-day endpoint. CTG exhibited identical macrophage phenotype distribution as native trachea, STG, and PDTG.

Understanding that synthetic materials may not only influence the quantity of infiltrating cells but the phenotype as well, we performed immunohistochemistry to characterize macrophage phenotype, since this was the most prevalent inflammatory cell in the implanted tracheal grafts. We found that the number of infiltrating macrophages (CD68+), and macrophage phenotype ratio (M1/M2, iNOS+/CD206+) did not differ between native, STG

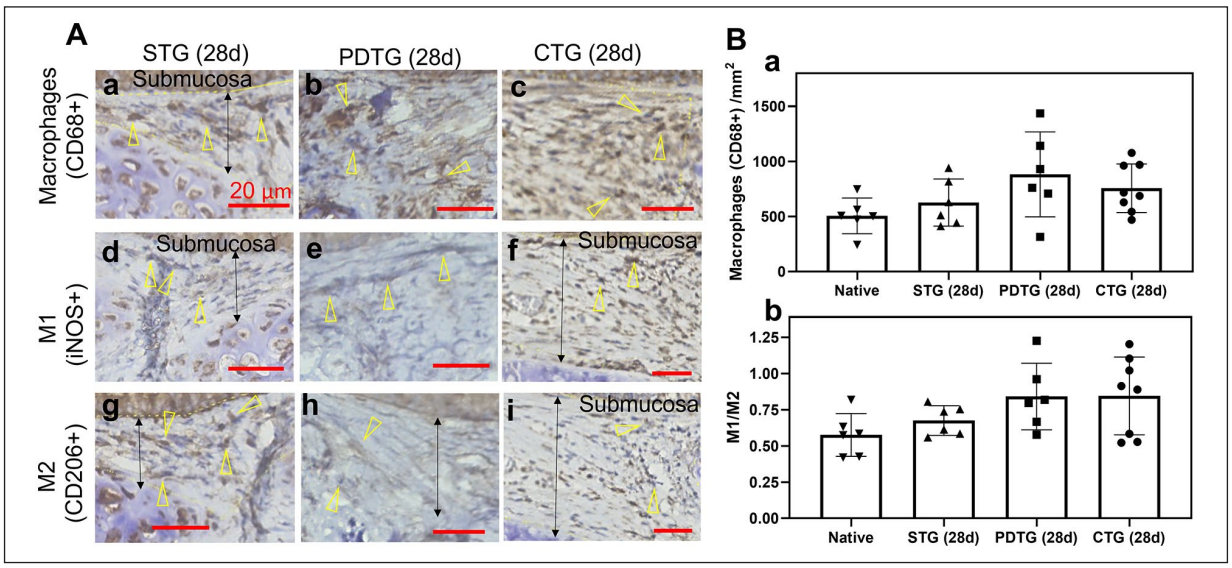

Figure 3. Macrophage infiltration and phenotype. (A) Infiltration of CD68+ macrophage (a–c), iNOS+ macrophage (d–f) and CD206+ macrophage (g–i) in STG (28d), PDTG (28d), and CTG (28d). Arrowheads denote CD68+, iNOS+, and CD206+ macrophages; arrows denote representative regions of submucosa where the cell number was quantified. (B) Quantification of macrophage (CD68+) infiltration in submucosa (a) and macrophage phenotype ratio (b).

(28d), PDTG (28d), and CTG (28d) (Figure 3). This finding confirmed that the splint is biocompatible and inert. Beyond its effects on graft biomechanics, the splint has minimal impact on the cellular microenvironment.

CTG and PDTG demonstrate equivalent graft epithelialization and endothelialization

We then assessed the host-derived regeneration of CTG and PDTG (Figure 4). Compared to PDTG (28d), CTG (28d) showed identical basal cell (Figure 4(a)), ciliated cell (Figure 4(b)), club cell (Figure 4(c)), and endothelial cell counts (Figure 4(d)). Overall basal cell quantity was similar between native, PDTG (28d), and CTG (28d). As expected, basal cell activation (K14+) was found to be higher in PDTG (28d) and CTG (28d) compared to native (Figure 4(a)). PDTG (28d) exhibited lower ciliated epithelial cell coverage (ACT+) compared to native (Figure 4(b)), but CTG (28d) was similar to native. Club cells (CCSP+) were lower in PDTG (28d) and CTG (28d) compared to native trachea (Figure 4(c)). Vascular endothelial (CD31+) cells were higher in PDTG (28d) and CTG (28d) compared to native (Figure 4(d)).

CTG does not increase submucosal thickness as observed in PDTG

Overall, tracheal graft implantation was found to increase submucosal thickness: STG, PDTG, and CTG submucosae were all found to be higher than native ($p=0.0265$, 0.0004, 0.0195, respectively) (Figure 5). When compared to control (STG), the submucosal thickness of PDTG was found to be higher ($p=0.0010$) which was not seen with CTG.

CTG eliminates graft cartilaginous collapse; airflow through grafts can also be attenuated by cellular infiltration and stenosis

Graft architecture was assessed with histological staining methods. Cartilaginous collapse was observed in 14.3% of PDTG (4/28). In contrast, no cartilaginous collapse was observed in CTG (0/8). Despite a lack of cartilaginous collapse, stenosis manifesting as cellular infiltration of the lamina propria was observed in 17.9% PDTG and 31.3% CTG (5/28 PDTG, 5/16 CTG, $p=0.1730$ Figure 6(a)).

Animals were scanned by microCT at days 0, 3, 7, and 28 after implantation (Figure 6). Graft diameter was found to remain stable in STG and CTG animals that survived to endpoint. However, a loss of graft diameter was seen in PDTG. Animals that survived to endpoint (STG (28d), PDTG (28d), and CTG (28d)) maintained graft patency, while animals requiring early euthanasia (EE) exhibited a loss of graft patency (*) that typically presented as respiratory distress (Figure 6(b)). Assessing graft function with computational fluid dynamics, resistance was higher in animals manifesting respiratory symptoms requiring early euthanasia.

Discussion

Partially decellularized tracheal grafts (PDTG) have demonstrated the capacity to support host-derived regeneration

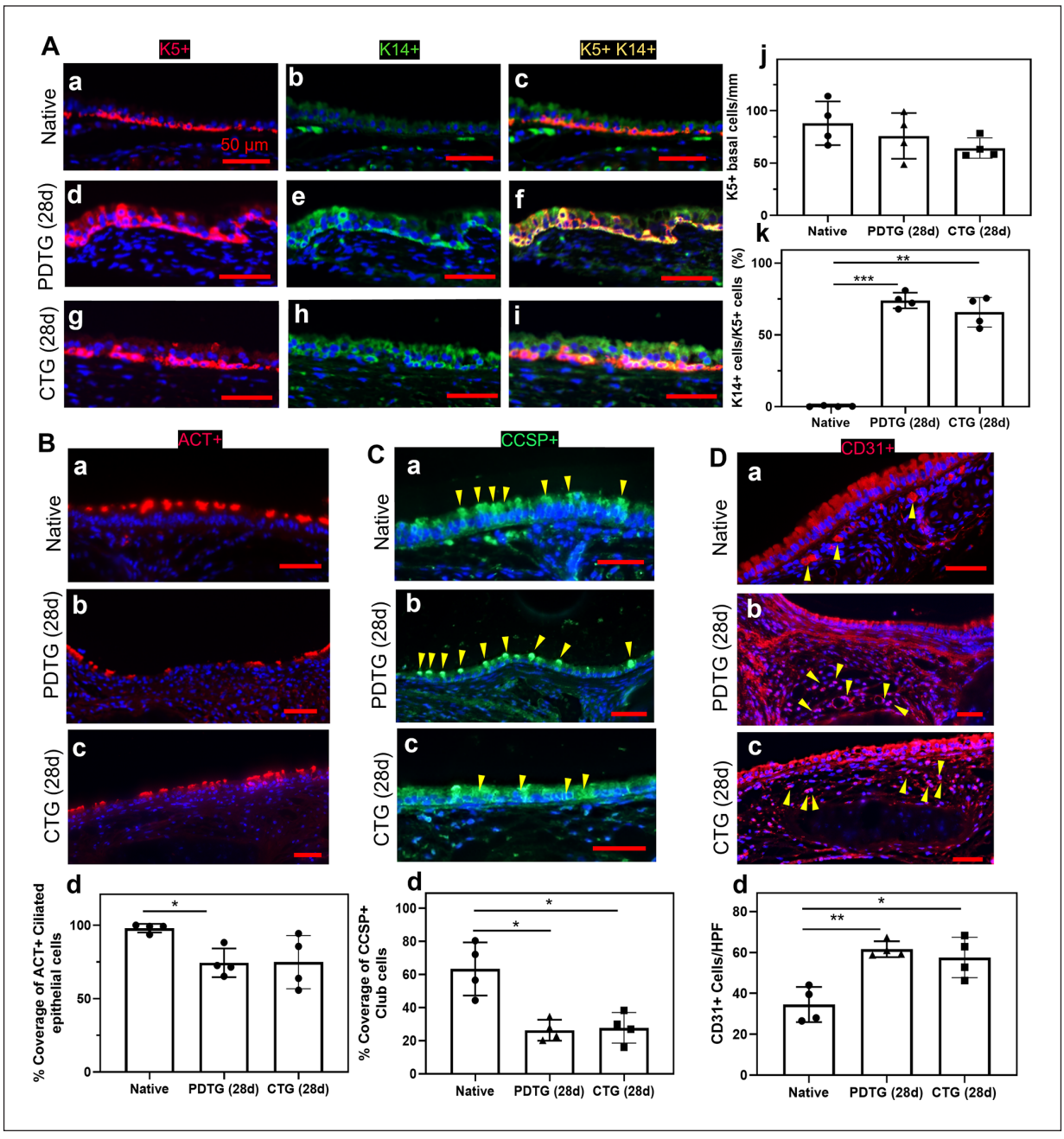

Figure 4. Epithelialization and endothelialization. (A) Representative images (a–i) and quantification (j and k) of basal cells (K5+K14+) in native trachea, PDTG, and CTG. * denotes a higher ratio of K5+K14+ basal cells over K5+ basal cells in DTS (28d) than native ($p = 0.0001$) and in CTG (28d) than native ($p = 0.0010$). (B) Representative ACT+ ciliated basal cell images (a–c) and quantification (d) of native trachea, PDTG (28d), and CTG (28d); * denotes lower ciliated basal cell coverage in PDTG (28d) than native trachea ($p = 0.0035$). (C) Representative club cell (CCSP+) images (a–c) and quantification (d) of native trachea, PDTG (28d) and CTG (28d); * denotes lower club cell coverage in PDTG (28d) and CTG (28d) than native trachea ($p = 0.0051$ and 0.0085). (D) Representative endothelial cell (CD31+) images (a–c) and quantification (d) of native trachea, PDTG (28d) and CTG (28d); * denotes lower higher endothelial cell regeneration in PDTG (28d) and CTG (28d) than native trachea ($p = 0.0012$ and 0.0126).

of an epithelium and microvasculature[7–9,34–37] while supporting chondrocyte viability.[7] When compared to conventional decellularization approaches that target the complete removal of all cell types, partial decellularization is more effective in preserving graft ECM and associated mechanical properties (Figure 1). Successful partial decellularization requires (1) the preservation of native basement membrane and cartilaginous ECM, (2) removal of all cells

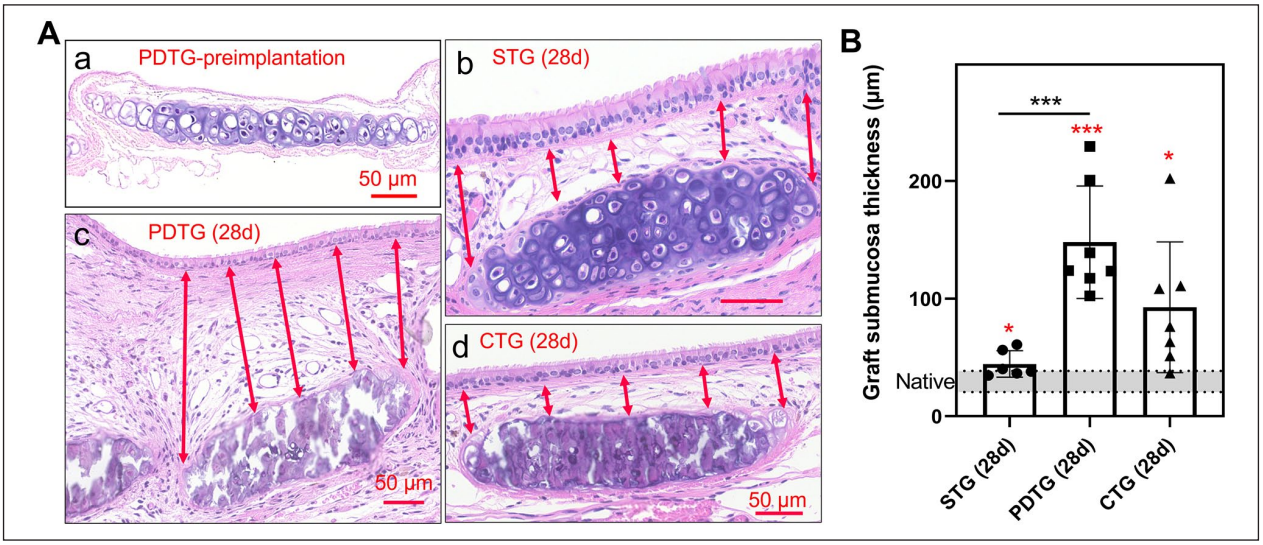

Figure 5. Histological analysis of submucosa thickness. (A) Representative H&E images of the submucosa region over one cartilage ring. (a) Preimplanted PDTG, (b) STG at day 28, (c) PDTG at day 28, (d) CTG at day 28. Arrows denote 5 measured submucosa thicknesses over one cartilage ring. (B) Quantification of submucosa thickness. * denotes higher submucosa thickness compared to native ($p = 0.0265$ for STG (28d), 0.0004 for PDTG (28d), 0.0195 for CTG (28d)), and significant higher submucosa thickness in PDTG than STG ($p = 0.0010$).

in the epithelium and epithelial submucosa including glandular, vascular, immune, and neural cell types, and (3) preservation of chondrocytes. Beyond its effect on graft mechanical properties, we found that complete decellularization of tracheal cartilage results in collateral damage to the basement membrane, potentially attenuating the affinity of the scaffold for epithelialization and neovascularization. For these reasons, we opted for an approach that is cartilage-sparing.[14,34,35,38–41] We confirmed that the creation of PDTG is feasible with the removal of highly immunogenic cell types, namely of the epithelium and endothelium, with preservation of chondrocytes.[7,42–44] These novel characteristics of PDTG improve the mechanical and biochemical properties when compared to completely decellularized constructs.

Understanding that repair and remodeling of a purely biologic graft can result in a transient change in graft mechanics, we explored the feasibility of Composite Tracheal Grafts (CTG): a graft composed of a biologic scaffold that has a high affinity for host-derived regeneration while imparting the consistent mechanical properties of a synthetic biomaterial. The blended nature of the composite graft would address the comparative loss of graft stiffness observed with the partial decellularization process.

We developed a 3D-printed tracheal splint that met generally accepted qualitative requirements: the splint (1) provided radial compressive mechanical support to keep the trachea open and patent, (2) allowed PDTG remodeling and development, (3) allowed growth and expansion of the airway, (4) did not interfere with the mucociliary architecture of the tracheal lumen, (5) was easily implantable, and (6) did not cause adverse tissue reaction or remodeling.[45–47] In this preliminary study, we selected surgical guide resin due to its biocompatibility and its ability to deliver consistent mechanical properties throughout the test period.[48,49] The splint did not increase macrophage infiltration, change macrophage phenotype, or attenuate graft epithelialization and endothelialization, resulting in similar submucosal thickening to syngeneic controls.[19,25] The effect of our splint on submucosal thickness could be attributed to changes in the micromechanical environment, limiting cell infiltration.[24,50,51] Further study of inflammatory cell types and populations in the lamina propria and their roles in submucosal thickening will be characterized based on ongoing work using single-cell RNA sequencing. In addition, future studies are devoted to the creation of a biodegradable splint that provides transient biomechanical support as intrinsic graft mechanics are restored through PDTG regeneration.

Several factors contributed to respiratory distress that required early euthanasia. First, the mouse model of orthotopic tracheal replacement has inherent challenges and is associated with perioperative morbidity[7,19,25,33] Additionally, a reduction in graft diameter leads to airway obstruction and respiratory symptoms. However, the specific histologic factors identified in the early euthanasia group were diverse, including both cartilaginous collapse and intraluminal stenosis. We found that CTG was able to attenuate cartilaginous collapse and did not result in an increase in submucosal thickness as seen in PDTG. The effect of CTG on cartilaginous collapse illustrated the potential benefit of composite grafts.

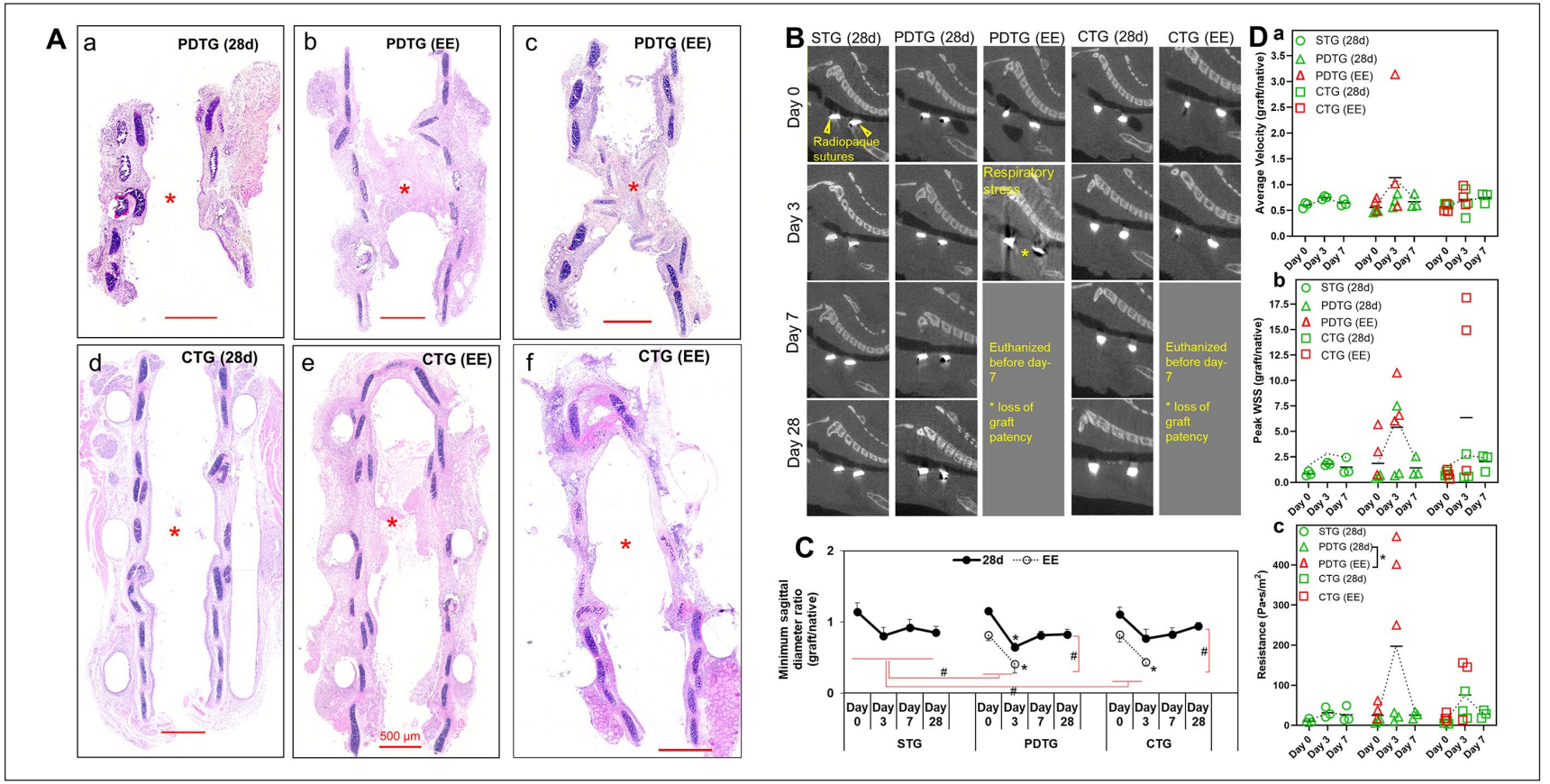

Figure 6. Graft patency and CFD characterization with time. (A) Representative H&E images of PDTG (28d) (a), PDTG (requiring Early Euthanasia, EE) (b and c), CTG (28d) (d), and CTG (EE) (e and f). * denote the graft patency in PDTG (28d) and CTG (28d), and stenosis in CTG (28d) and CTG (EE). (B) Representative sagittal reconstructions of microCT images of STG (28d), PDTG (28d), PDTG (EE), CTG (28d), and CTG (EE) at days 0, 3, 7, and 28. Yellow arrowheads highlight radiopaque sutures that identify the proximal (left) and distal anastomosis (right). A yellow asterisk denotes loss of graft patency. (C) Quantification of the sagittal diameter of the graft normalized by comparing to a corresponding host native airway sagittal diameter. * represent decreased sagittal diameter at day 3 compared to day 0 of PDTG (28d), PDTG (EE), and CTG (EE) ($p < 0.0001$, $p = 0.0256$ and 0.0212, respectively). # represent the significant overall lower sagittal diameter of PDTG (EE) than PDTG (28d) ($p = 0.0012$), CTG (EE) than CTG (28d) ($p = 0.0047$), PDTG (EE) than STG (28d) ($p = 0.0002$), CTG (EE) than STG (28d) ($p = 0.0019$). (D) CFD modeling of tracheal graft airflow metrics including: (a) average velocity, (b) peak wall shear stress, (c) resistance ($Pa \cdot s/m^2$); * denotes higher resistance in PDTG (28d) compared to PDTG (EE) ($p = 0.0313$).

There were several limitations to this study. First, a mouse model of orthotopic tracheal transplant did not allow for a complete assessment of all clinical manifestations that may be observed in a large animal or human trial as the small scale of the surgical model amplifies the morbidity of any airway narrowing. Second, the mechanisms of the loss of stiffness in PDTG and the development of stenosis in some grafts and not others remain unclear.

Conclusion

We created a composite tracheal graft (CTG) that integrated external support of partially decellularized tracheal grafts with 3D-printed splints to confer consistent mechanical properties during tracheal repair and renewal. We found that evaluating CTG performance in a mouse model of orthotopic transplant is highly feasible, which will benefit the in vivo assessment of other biomaterials for airway reconstruction. Composite Tracheal Grafts exhibited sustained regeneration and preserve mechanically-stable graft cartilage, creating a potential solution for long-segment tracheal replacement.

Acknowledgements

We would like to express gratitude to the animal care and veterinary staff, the Morphology Core, and Terri Shaffer from the Small Animal Imaging Facility (SAIF) at the Abigail Wexner Research Institute at Nationwide Children's Hospital.

Declaration of conflicting interests

The author(s) declared no potential conflicts of interest with respect to the research, authorship, and/or publication of this article.

Funding

The author(s) disclosed receipt of the following financial support for the research, authorship, and/or publication of this article: The work presented is funded by the National Institutes of Health (NIH NHLBI K08HL138460, NIH NHLBI R01HL157039 TC).

ORCID iD

Lumei Liu https://orcid.org/0000-0001-9849-6881

Supplemental material

Supplemental material for this article is available online.

References

1. Kolb F, Simon F, Gaudin R, et al. 4-Year follow-up in a child with a total autologous tracheal replacement. *New Engl J Med* 2018; 378: 1355–1357.
2. Martinod E, Chouahnia K, Radu DM, et al. Feasibility of bioengineered tracheal and bronchial reconstruction using stented aortic matrices. *JAMA* 2018; 319: 2212–2222.
3. Delaere P, Lerut T and Van Raemdonck D. Tracheal transplantation: state of the art and key role of blood supply in its success. *Thorac Surg Clin* 2018; 28: 337–345.
4. Chiang T, Pepper V, Best C, et al. Clinical translation of tissue engineered trachea grafts. *Ann Otol Rhinol Laryngol* 2016; 125: 873–885.
5. Hodde JP, Badylak SF, Brightman AO, et al. Glycosaminoglycan content of small intestinal submucosa: a bioscaffold for tissue replacement. *Tissue Eng* 1996; 2: 209–217.
6. Choe JA, Jana S, Tefft BJ, et al. Biomaterial characterization of off-the-shelf decellularized porcine pericardial tissue for use in prosthetic valvular applications. *J Tissue Eng Regen Med* 2018; 12: 1608–1620.
7. Liu L, Dharmadhikari S, Shontz KM, et al. Regeneration of partially decellularized tracheal scaffolds in a mouse model of orthotopic tracheal replacement. *J Tissue Eng* 2021; 12: 20417314211017417.
8. Elliott MJ, Butler CR, Varanou-Jenkins A, et al. Tracheal replacement therapy with a stem cell-seeded graft: lessons from compassionate use application of a GMP-compliant tissue-engineered medicine. *Stem Cells Transl Med* 2017; 6: 1458–1464.
9. Kutten JC, McGovern D, Hobson CM, et al. Decellularized tracheal extracellular matrix supports epithelial migration, differentiation, and function. *Tissue Eng Part A* 2015; 21: 75–84.
10. Elliott MJ, De Coppi P, Speggiorin S, et al. Stem-cell-based, tissue engineered tracheal replacement in a child: a 2-year follow-up study. *Lancet* 2012; 380: 994–1000.
11. Hamilton NJ, Kanani M, Roebuck DJ, et al. Tissue-engineered tracheal replacement in a child: A 4-year follow-up study. *Am J Transplant* 2015; 15: 2750–2757.
12. Adkisson HD, Milliman C, Zhang X, et al. Immune evasion by neocartilage-derived chondrocytes: implications for biologic repair of joint articular cartilage. *Stem Cell Res* 2010; 4: 57–68.
13. Chesterman P and Smith AU. Homotransplantation of articular cartilage and isolated chondrocytes: an experimental study in rabbits. *J Bone Joint Surg Br* 1968; 50: 184–197.
14. Aoki FG, Varma R, Marin-Araujo AE, et al. De-epithelialization of porcine tracheal allografts as an approach for tracheal tissue engineering. *Sci Rep* 2019; 9: 12034.
15. Cui P, Liu P, Li S, et al. De-epithelialized heterotopic tracheal allografts without immunosuppressants in dogs: long-term results for cartilage viability and structural integrity. *Ann Otol Rhinol Laryngol* 2021; 130: 441–449.
16. Dang LH, Tseng Y, Tseng H, et al. Partial decellularization for segmental tracheal scaffold tissue engineering: a preliminary study in rabbits. *Biomolecules* 2021; 11: 866.
17. Pepper V, Best CA, Buckley K, et al. Factors influencing poor outcomes in synthetic tissue-engineered tracheal replacement. *Otolaryngol Head Neck Surg* 2019; 161: 458–467.
18. Greaney AM and Niklason LE. The history of engineered tracheal replacements: interpreting the past and guiding the future. *Tissue Eng Part B Rev* 2021; 27: 341–352.
19. Dharmadhikari S, Liu L, Shontz K, et al. Deconstructing tissue engineered trachea: assessing the role of synthetic scaffolds, segmental replacement and cell seeding on graft performance. *Acta Biomater* 2020; 102: 181–191.
20. Danielson A, Liu L, Shontz KM, et al. Spatial and temporal analysis of host cells in tracheal graft implantation. *Laryngoscope* 2021; 131: E340–E345.

21. James IA, Yi T, Tara S, et al. Hemodynamic characterization of a mouse model for investigating the cellular and molecular mechanisms of neotissue formation in tissue-engineered heart valves. *Tissue Eng Part C Methods* 2015; 21: 987–994.
22. Qiagen AG. *Dneasy© blood and tissue handbook*. Hombrechtikon: Qiagen AG, 2006.
23. Zopf DA, Hollister SJ, Nelson ME, et al. Bioresorbable airway splint created with a three-dimensional printer. *New Engl J Med* 2013; 368: 2043–2045.
24. Liu L, Stephens B, Bergman M, et al. Role of collagen in airway mechanics. *Bioengineering* 2021; 8: 13.
25. Tan ZH, Dharmadhikari S, Liu L, et al. Tracheal macrophages during regeneration and repair of long-segment airway defects. *Laryngoscope* 2022; 132: 737–746.
26. Florez-Sampedro L, Song S and Melgert BN. The diversity of myeloid immune cells shaping wound repair and fibrosis in the lung. *Regeneration* 2018; 5: 3–25.
27. Lohrmann F, Forde AJ, Merck P, et al. Control of myeloid cell density in barrier tissues. *FEBS J* 2021; 288: 405–426.
28. Birchall MA, Ayling SM, Harley R, et al. Laryngeal transplantation in minipigs: early immunological outcomes. *Clin Exp Immunol* 2012; 167: 556–564.
29. Davis RJ and Hillel AT. Inflammatory pathways in the pathogenesis of iatrogenic laryngotracheal stenosis: what do we know? *Transl Cancer Res* 2020; 9: 2108–2116.
30. Ghosh A, Malaisrie N, Leahy KP, et al. Cellular adaptive inflammation mediates airway granulation in a murine model of subglottic stenosis. *Otolaryngol Head Neck Surg* 2011; 144: 927–933.
31. De Kleer I, Willems F, Lambrecht B, et al. Ontogeny of myeloid cells. *Front Immunol* 2014; 5: 423.
32. Engler AE, Ysasi AB, Pihl RMF, et al. Airway-associated macrophages in homeostasis and repair. *Cell Rep* 2020; 33: 108553.
33. Dharmadhikari S, Best CA, King N, et al. Mouse model of tracheal replacement with electrospun nanofiber scaffolds. *Ann Otol Rhinol Laryngol* 2019; 128: 391–400.
34. Remlinger NT, Czajka CA, Juhas ME, et al. Hydrated xenogeneic decellularized tracheal matrix as a scaffold for tracheal reconstruction. *Biomaterials* 2010; 31: 3520–3526.
35. Hung SH, Su CH, Lin SE, et al. Preliminary experiences in trachea scaffold tissue engineering with segmental organ decellularization. *Laryngoscope* 2016; 126: 2520–2527.
36. Xu Y, Li Y, Liu Y, et al. Surface modification of decellularized trachea matrix with collagen and laser micropore technique to promote cartilage regeneration. *Am J Transl Res* 2019; 11: 5390–5403.
37. Sun F, Pan S, Shi HC, et al. Structural integrity, immunogenicity and biomechanical evaluation of rabbit decellularized tracheal matrix. *J Biomed Mater Res A* 2015; 103: 1509–1519.
38. Conconi MT, De Coppi P, Di Liddo R, et al. Tracheal matrices, obtained by a detergent-enzymatic method, support in vitro the adhesion of chondrocytes and tracheal epithelial cells. *Transpl Int* 2005; 18: 727–734.
39. Haykal S, Soleas JP, Salna M, et al. Evaluation of the structural integrity and extracellular matrix components of tracheal allografts following cyclical decellularization techniques: comparison of three protocols. *Tissue Eng Part C Methods* 2012; 18: 614–623.
40. Johnson C, Sheshadri P, Ketchum JM, et al. In vitro characterization of design and compressive properties of 3D-biofabricated/decellularized hybrid grafts for tracheal tissue engineering. *J Mech Behav Biomed Mater* 2016; 59: 572–585.
41. Den Hondt M, Vanaudenaerde BM, Maughan EF, et al. An optimized non-destructive protocol for testing mechanical properties in decellularized rabbit trachea. *Acta Biomater* 2017; 60: 291–301.
42. Cleven HA, Genden EM and Moran TM. Reepithelialized orthotopic tracheal allografts expand memory cytotoxic T lymphocytes but show no evidence of chronic rejection. *Transplantation* 2005; 79: 861–868.
43. Richards DM, Dalheimer SL, Hertz MI, et al. Trachea allograft class I molecules directly activate and retain CD8+ T cells that cause obliterative airways disease. *J Immunol* 2003; 171: 6919–6928.
44. Genden EM, Iskander A, Bromberg JS, et al. The kinetics and pattern of tracheal allograft re-epithelialization. *Am J Respir Cell Mol Biol* 2003; 28: 673–681.
45. Zopf DA, Hollister SJ, Nelson ME, et al. Bioresorbable airway splint created with a three-dimensional printer. *New Engl J Med* 2013; 368: 2043–2045.
46. Zopf DA, Flanagan CL, Wheeler M, et al. Treatment of severe porcine tracheomalacia with a 3-dimensionally printed, bioresorbable, external airway splint. *JAMA Otolaryngol Head Neck Surg* 2014; 140: 66–71.
47. Hollister SJ, Flanagan CL, Zopf DA, et al. Design control for clinical translation of 3D printed modular scaffolds. *Ann Biomed Eng* 2015; 43: 774–786.
48. Annibali S, La Monaca G, Tantardini M, et al. The role of the template in prosthetically guided implantology. *J Prosthodont* 2009; 18: 177–183.
49. Salem D. Surgical guides for dental implants; a suggested new classification. *J Dent Oral Health* 2019; 6: 1–8.
50. Nicolas J, Magli S, Rabbachin L, et al. 3D extracellular matrix mimics: fundamental concepts and role of materials chemistry to influence stem cell fate. *Biomacromolecules* 2020; 21: 1968–1994.
51. Li R, Liu K, Huang X, et al. Bioactive materials promote wound healing through modulation of cell behaviors. *Adv Sci* 2022; 9: e2105152.